

MEASUREMENT AND CHARACTERIZATION METHODS IN FUNCTIONAL THIN FILM DEPOSITION IN PLASMA SPUTTERING FOR MATERIAL PROCESSING

^{1,3*}MD. AMZAD HOSSAIN, ^{2,3}MD ABDUL MAJED PATWARY, ¹FATEMA TUZ ZAHURA and ¹MD. MUSTAFIZUR RAHMAN,

¹Department of Electrical and Electronic Engineering, Jashore University of Science and Technology, Jashore -7408, Bangladesh

²Department of Chemistry, Comilla University, Cumilla -3506, Bangladesh

³Graduate School of Science and Engineering, Saga University, Saga, 840-8502, Japan

ABSTRACT:

This study discussed the experimental methods as well as measurement techniques used in functional thin film characterization. Various kinds of measurement tools and diagnostics were represented and well discussed. Material characterization methods were used to analyze the structure of the fabricated crystal, chemical composition, thickness, surface morphology, conductivity, as well as its optical properties. Each of the measurement and characterization techniques was explained. The evaluation of the prepared functional film was analyzed by some useful technical tools such as surface profiler, four-point probe method, atomic force microscopy (AFM), scanning force microscopy (SEM), Raman spectroscopy, X-ray diffraction (XRD), Ultraviolet Visible Near-Infrared (UV-Vis-NIR) spectroscopy. A Langmuir probe was used to measure ion saturation current and for estimation of plasma density. Furthermore, the simulation analysis techniques used for the magnetized plasma sputtering source were also presented.

Keywords: Thin film, Plasma sputtering, Material processing, Thickness, Resistivity, AFM, SEM, XRD, UV-Vis-NIR

1. Introduction

Plasma is the fourth state of matter, generally consisting of positive ions and free electrons [1]. Plasma and its particles play an effective role in nanotechnology and manufacturing industries in the world [1-4]. Various kinds of plasma sources have been developed for material processing and industrial applications [5-25]. Plasma sources are widely used in the microelectronic industry, functional thin film deposition, magnetic films, additive materials processing, surface treatment and cleaning, flat panel display fabrication, transparent conductive oxides film preparation, solar cell, and many other rapidly growing areas [1-25]. It is necessary to discuss various measurement and characterization methods for functional thin film deposition in plasma sputtering sources. This study discusses various measurement and characterization techniques used in plasma sources for material processing and industrial applications.

2. Major Experimental Apparatus in RF magnetized Plasma Sputtering

The major apparatuses used to do the experiments utilized in RF magnetized plasma sputtering research, showing matching network, vacuum system, external motor circuits, oscilloscope, and plasma discharge chamber was shown in Fig. 1[4]. The experiments were performed in a stainless-steel cylindrical vacuum chamber with an outer diameter of 235 mm, an inner diameter of 160 mm and a height of 195 mm. The discharge chamber was evacuated to a base pressure of 10^{-5} Pa by a turbo molecular and an oil rotary pump [1-3]. By regulating a flow meter, argon (Ar) gas was employed as a sputtering gas. An RF power source at 13.56 MHz was applied to the target via an impedance matching network. A copper plate of 3 mm thickness was used as the target to measure the sputtering characteristics. An aluminum disc was used to measure plasma parameters in order to avoid thin film deposition on the Langmuir probe. The discharge voltage between the RF powered electrode and the grounded vacuum wall was measured by a high-voltage probe connected to an oscilloscope [4].

The iron yoke was set up with a gap of 1 mm, and 0 mm from the copper target plate for the rotational and stationary modes, respectively. The circular iron yoke disk with the magnet arrangement was rotated by an iron yoke shaft powered by an external motor. The two-dimensional magnetic flux distributions were simulated using the poissonsuperfish [5]. A precision surface tool was used to measure the erosion depth of the copper target as a basis for calculating the target utilization percentage. The time-averaged ion saturation currents were measured to obtain the ion flux to the target by a tiny tungsten wire probe of 1.0 mm in diameter and 10 mm in length. In order to avoid the influence of the RF potential oscillations on the probe current-voltage characteristics, the probe wire was connected to an LC filter circuit [1-2]. The ion flux to the target was calculated from the ion saturation current by negatively biasing the probe with a resistance of 100 Ω [1-4].

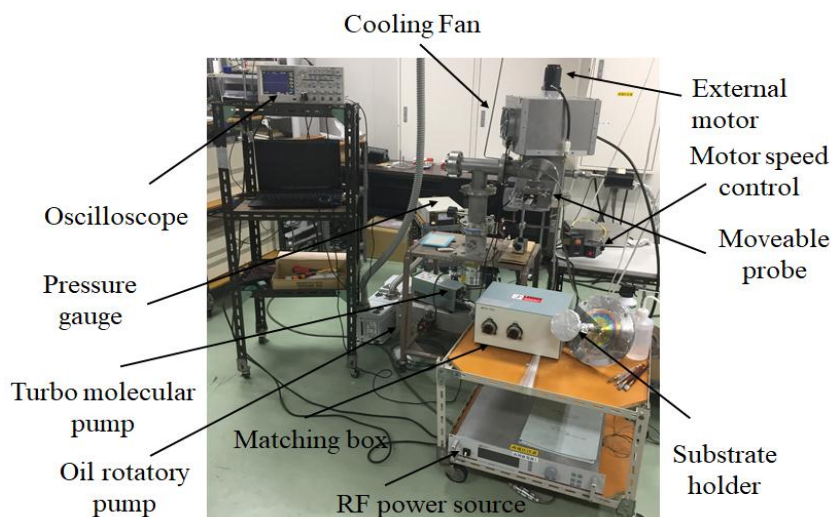


Figure 1. The major apparatuses used to do the experiments in this research showing matching network, vacuum system, external motor circuits, oscilloscope, and discharge chamber.

3. Ion Saturation Current, Plasma Density and Electron Temperature Measurement

Figure 2 shows ion saturation current and current-voltage characteristics measuring equipment. A Langmuir probe and a DC power supply were used [4]. The biasing voltages were changed from -70 V to +70 V. The Langmuir probe was compensated with an LC parallel filter circuit to avoid the influence of the RF plasma potential fluctuations on the probe's current-voltage characteristics. The probe measurements were carefully performed to minimize disturbance to the stable plasma [1-3].

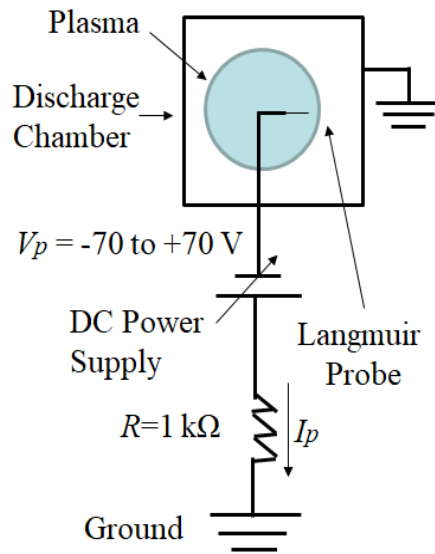


Figure 2. Ion saturation current and current-voltage characteristics measuring equipment.

Figure 3 shows a practical current-voltage characteristics curve showing its various parts[4]. The point at which the curve crosses the V axis is called the floating potential V_f . At any potential, where electron saturation starting current is defined as V_p . The electron temperatures and the plasma density were estimated using the current-voltage characteristics curve. According to the probe theory [1-2], the ion saturation current is proportional to the ion flux to the target. Moreover, the plasma density can be estimated from ion saturation, which can be expressed in the following eq. (1).

$$I_{isat} = 0.6 qAn \left(\frac{KT_e}{M} \right)^{1/2} \quad (1)$$

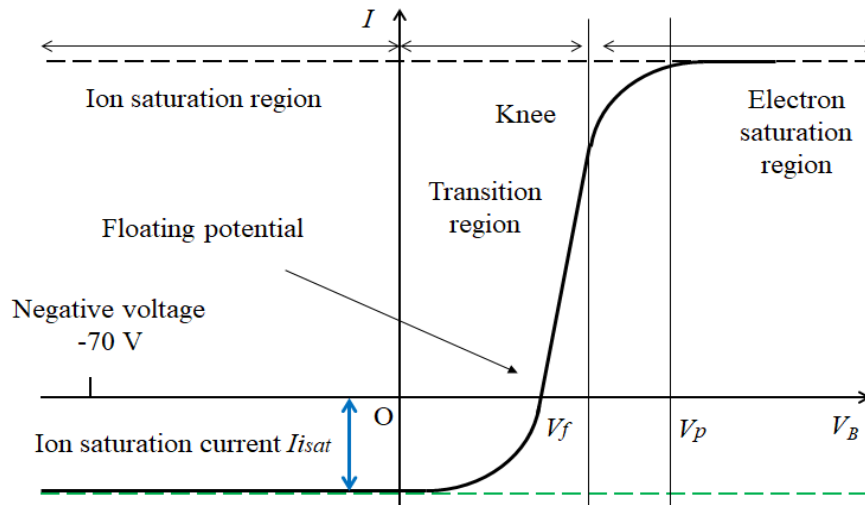


Figure 3. A practical current-voltage characteristics curve showing its various parts.

At floating potential, electron and ion currents are equal, that is, $I_e = I_i$. So that the total current is zero. The electron current can be expressed as eq. (2). Taking logarithm and simplifying eq. (2), it can be written in the following form in eq. (4) and (5). As a result, the inverse slope of the logarithmic electron probe current with respect to biasing voltage, V_B (in volts), gives the electron temperature, T_e directly.

$$I_e = I_{esat} \exp \exp\left(\frac{V_B - V_P}{T_e}\right) \quad (2)$$

$$\frac{I_e}{I_{esat}} = \exp \exp\left(\frac{V_B - V_P}{T_e}\right) \quad (3)$$

$$\ln \ln\left(\frac{I_e}{I_{esat}}\right) = \frac{V_B - V_P}{T_e} \quad (4)$$

$$T_e = \frac{V_B - V_P}{\ln \ln\left(\frac{I_e}{I_{esat}}\right)} \quad (5)$$

The measurement of ion saturation current, I_{isat} is the simplest and best way to determine the plasma density, n . Plasma sheath around a negatively biased probe is so thin that the area of the sheath edge is essentially the same as the area of the probe tip itself at higher plasma densities than 10^{16} m^{-3} . Equation (1) indicates a constant ion saturation current, which can occur only for flat probes in which the sheath area cannot increase as the probe functions more and more negatively. In practice, ion saturation current, I_{isat} usually has a slope to it because the I_{isat} has to come from a disturbed volume of plasma (the presheath). Plasma density can be calculated from the following Eq. (7).

$$I_{isat} = 0.6 qnA \left(\frac{KT_e}{M} \right)^{1/2} \quad (6)$$

$$n = \frac{I_{isat}}{0.6 qA \left(\frac{KT_e}{M} \right)^{1/2}} \quad (7)$$

4. Measurement of the Target Erosion Depth and Target Utilization Rate

A precision surface profile tool (Mitutoyo SJ-400) was used to measure the radial profile of the thickness of the deposited Cu film. Figure 4 shows the target erosion depth and film thickness measuring apparatuses showing the eroded target and moving step profiler[4]. For erosion depth measurement, measurements are carried out using a step meter (Mitutoyo SJ-400). A precision tape was attached to a part of the target material. The target material was set for the experiment for plasma sputtering. After the experiment, the tape was taken off. The mechanical step at the tape boundary between the tape part and the sputtered part was used to measure the difference. Scanning was done in a direction perpendicular to the target surface. It was scanning in the direction of the erosion surface from the part where it was eroded. The thin film thickness is obtained from the output data obtained by the stylus profilometer. In fact, it captures the fine unevenness of the material surface with high definition.

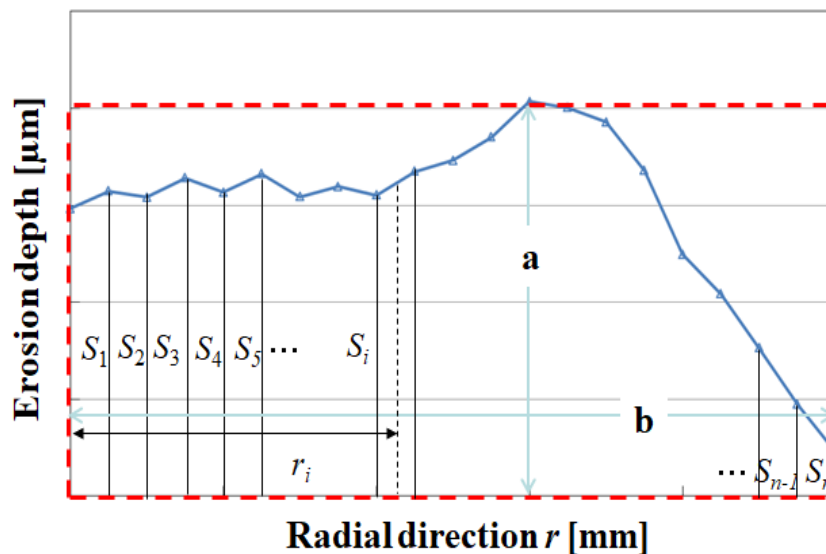


Figure 4. Target erosion depth profiles and calculation of the target utilization percentage.

The target utilization percentage was estimated based on the ratio of the target erosion volume to the volume calculated under the assumption that the target was completely eroded at a maximum erosion depth [4]. In Fig. 4, the target erosion depth profiles and the calculation of the target utilization percentage were shown[4]. The target utilization percentage was calculated using the following eq. (8). Fig. 5 shows the target erosion depth and film thickness measuring devices showing the

eroded target and moving step profiler [4]. A computer was interfacing with a moving step profiler to get the eroded thickness.

$$T_U = \left(\sum_{i=1}^n 2\pi r_i S_i / (\pi a b^2) \right) \times 100 [\%] \quad (8)$$

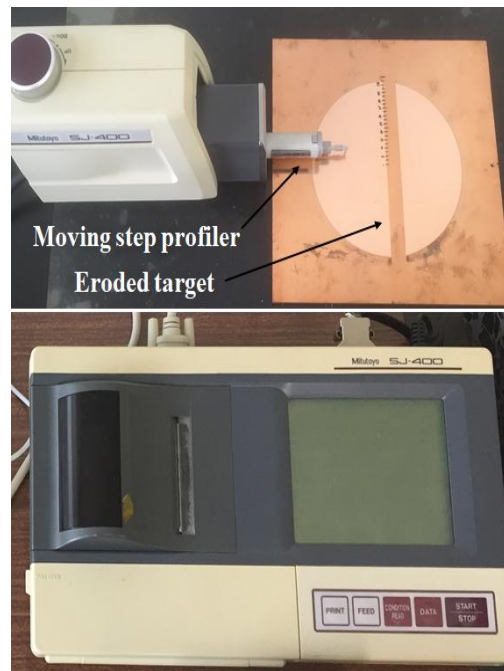


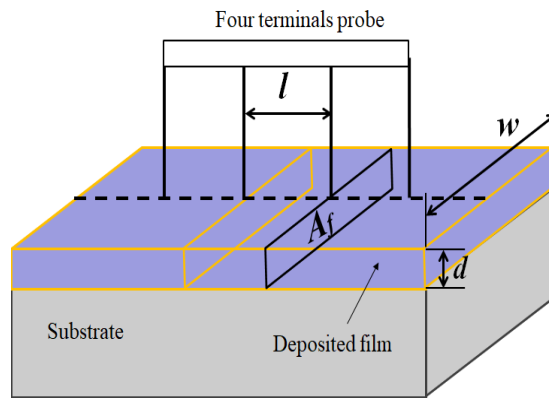
Figure 5. Target erosion depth and film thickness measuring apparatuses showing the eroded target and moving step profiler.

5. Resistivity of the Prepared Film

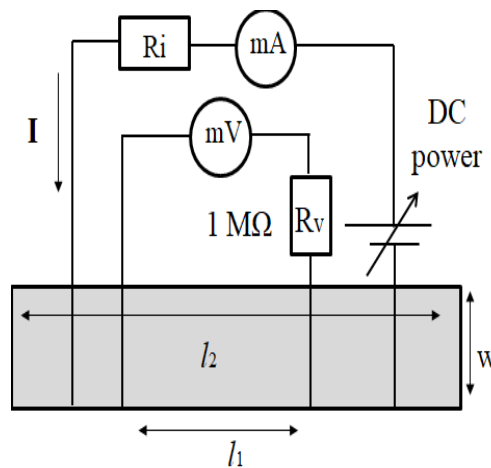
The resistivity of the deposited films was measured by a standard four terminals probe method at room temperature. Separate pairs of current-carrying and voltage-sensing electrodes were used to make more accurate measurements by the four-terminal probe method. Figure 6 shows four-terminal probe methods to measure deposited film resistivity mentioning (a) schematic diagram and (b) electrical circuit diagram [4]. The deposited film resistance can be calculated using the current voltage characteristics curve. However, the film resistance is expressed by the following eq. (9), where A_f is the deposited film surface. The resistivity, ρ can be calculated using eq. (10), where R_f is the resistance of the prepared functional film.

$$R_f = \rho \frac{l}{A_f} \quad (9)$$

$$\rho = R_f \frac{d \times w}{l} \quad (10)$$



(a)



(b)

Figure 6. Four terminals probe method to measure deposited film resistivity (a) schematic diagram and (b) electrical circuit diagram.

6. X-ray diffraction (XRD)

XRD was used as a fast non-destructive analytical tool for the phase recognition of crystalline nanomaterials. It can reveal true evidence on unit cell dimensions. One can simply attain the data of the crystallographic structure, composition, and physical

properties of the measured sample through the scattered intensity of an X-ray beam striking into a sample as a function of incident angle. The general working principle and schematic view of XRD was shown in Figure 7. Here, $RQ = QP = d \sin \theta$ (from the Fig. 7). So, the difference in path length $= RQ + QP = 2d \sin \theta$ must be an integral number of wavelengths, $n\lambda = 2d \sin \theta$ ($n = 1, 2, 3, \dots$), which is well known as Bragg's equation. For a cubic system, $d_{hkl}^2 = \frac{a^2}{h^2 + k^2 + l^2}$, where a is the lattice spacing of the cubic crystal, and h , k , and l are the Miller indices of the Bragg plane. The lattice constants can be found using the equation. By applying the equation, one can determine the present phases in any crystalline or polycrystalline materials.

The system can be effectively used for comprehensive structural analysis of plasma grown materials such as advanced semiconductors, nanomaterials[6, 7] and thin films [8, 9]. It controls a widespread variety of X-ray scattering applications such as high-resolution diffraction, in-plane diffraction, reflectivity, wafer mapping, thin film phase analysis, grazing incidence, small angle X-ray scattering, texture, stress, and non-ambient analysis. The identification of the phases was accomplished by the assessment of the XRD diffractogram with the international center for diffraction data base.

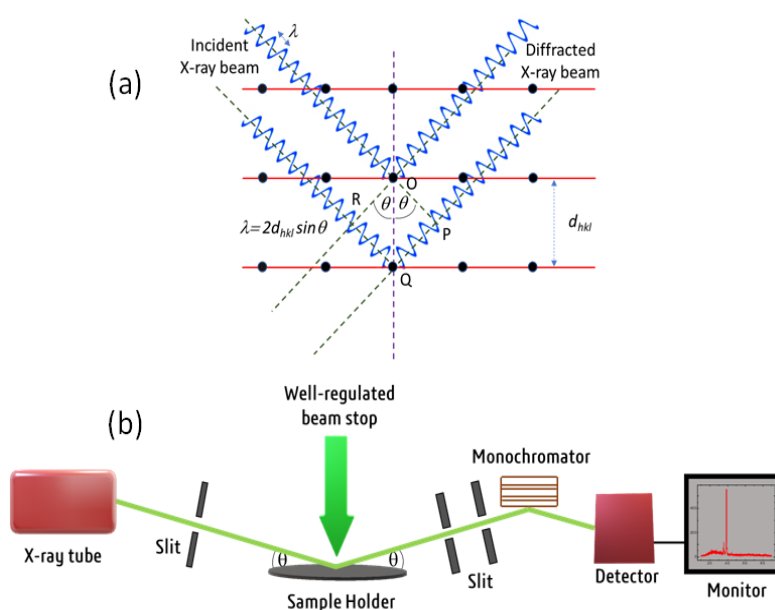


Figure 7. Schematic view of X-ray diffraction spectroscopy

7. Raman spectrophotometer

The schematic view of the Raman spectrometer is displayed in Figure 8. An Indian physicist C. V. Ramandev developed Raman spectroscopy, which is a spectroscopic technique usually applied to determine vibrational modes of molecules, although rotational and other low-frequency modes of systems may also

be detected [10]. Raman spectroscopy is usually applied in chemistry to distribute a structural fingerprint by which molecules can be recognized. It is a good complementary technique to regulate the phase existing in the film [8, 11]. Generally, the spectra were documented in the backscattering geometry at room temperature. A polarized 325, 448 or 532 nm excitation laser was focused onto the sample surface using a 200 x objective.

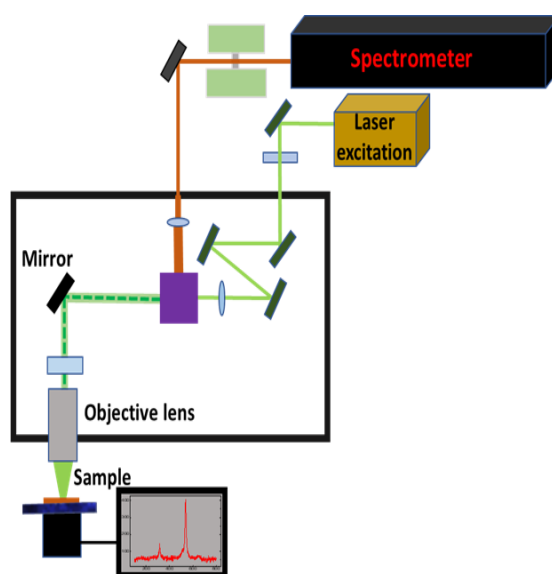


Figure 8. Schematic view of Raman spectrometer.

8. Scanning electron microscopy (SEM)

Morphological characterization of the surface or cross-sectional morphology of the deposited layers grown by chemical [12, 13] and physical [8] processes could be assessed by SEM analysis. The schematic view of the SEM is represented in Figure 9. The system can be controlled both at a high accelerating voltage of 30 kV and a low accelerating voltage of 200 V. The SEM resolution could be managed as required. The crystallite grain size, shape as well as orientation of various compounds could be investigated by this apparatus.

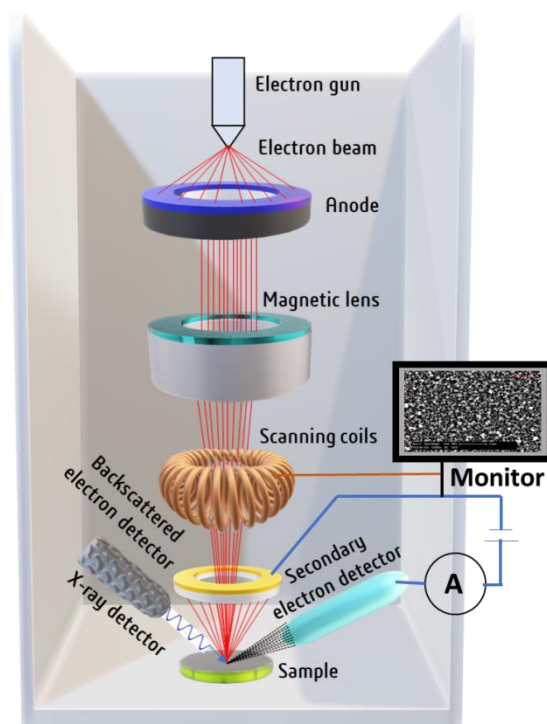


Figure 9: Schematic view of Secondary Electronic Microscopy

9. Atomic force microscopy (AFM)

Atomic force microscopy (AFM) scanning was performed to observe the surface morphology of the prepared thin films. To distinguish the surface morphology of the plasma deposited films [8, 14], AFM is effectively used in plasma research. It is complementary to SEM as shown in Figure 10. It is constructed for imaging samples having around 1.5 cm diameter. By applying a series of interchangeable scanners, it can deliver images from the atomic scale to 175 μm in size. During measurement by the AFM, a sharp probe (tip) is applied to scan the surface of the sample by calculating forces between the surface and the probe at a very short space. The topographic appearance of the surface is shaped by recording the differences of the probe altitude above the surface while the probe is scanned constantly across the surface. The crystallite grain size, shape as well as alignment of different compounds are studied by this apparatus.

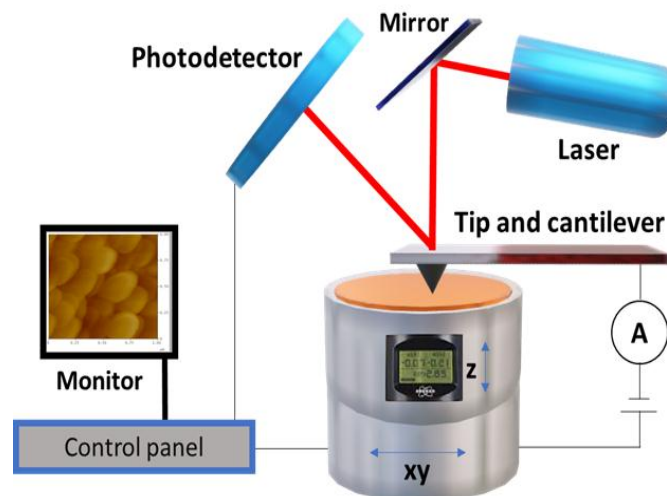


Figure 10. Schematic view of Atomic Force Microscopy

10. UV-Vis-NIR spectrophotometer

The transmittance and reflectance spectra of the plasma grown films [8, 14] could be measured using a UV-Vis-NIR spectrophotometer. A schematic view of the UV-Vis-NIR spectrophotometer is represented in Figure 11. It is a double beam system with a single monochromatic light source. The wavelength range could be generally maintained in between 190–2000 nm with a wavelength accuracy of 1.5 nm.

Optical absorption is measured from the absorption coefficient (α) of the thin films which is derived from the following equation using transmittance and reflectance calculated by a double-beam spectrophotometer in the wavelength range of 200 – 2000 nm.

$$\alpha(\lambda) = -\frac{1}{t} \ln \left\{ \frac{1}{2R(\lambda)^2} \left[\sqrt{\frac{(1-R(\lambda))^4}{T(\lambda)^2} + 4R(\lambda)^2} - \frac{(1-R(\lambda))^2}{T(\lambda)} \right] \right\} \quad \text{--- (1)}$$

where, t = thickness, α = absorption coefficient, R = reflectivity and T = transmittance.

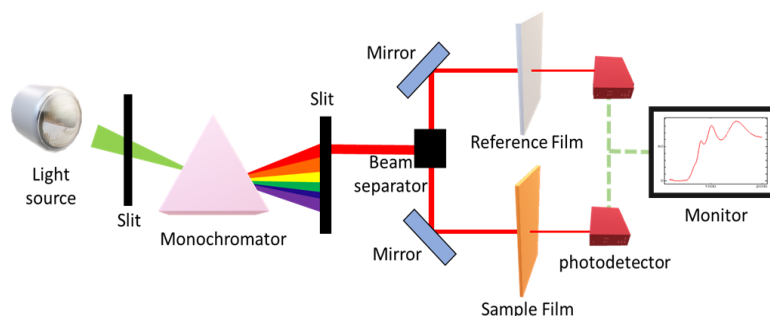


Figure 11. Schematic view of the UV-Vis-NIR spectrophotometer.

11. Magnetic Field Analysis Simulation

Many researchers simulated the two-dimensional and three-dimensional magnetic field in the proposed plasma sources [15-25]. The two-dimensional magnetic flux lines and their density profiles (B_x and B_z) are analyzed by conventional Electromagnetic field analysis software poissonsuperfish [26] developed at Los Alamos National Laboratory. It was analyzed by selecting the dimensions and the magnetic properties of the permanent magnet. It was created as input coding that runs on Poisson Superfish with TeraPad. It was analyzed by creating a mesh area by command Automesh, and WEF plot command for display of mesh creation and confirmation. Magnetic field analysis was performed by commanding Pandira. Output electronic text format data of the magnetic field was made by the commanding SF 7. Using MS Excel text format data was analyzed, and horizontal, B_x , and vertical, B_z magnetic field density profiles were evaluated. Moreover, three-dimensional (3D) magnetic flux lines for the proposed magnet setups and their flux distributions were analyzed using Femtet software to observe the effects of the magnetic field profiles.

Conclusion

Various plasma sources and their applications were discussed. Few technical tools such as surface profiler, four-point probe method, atomic force microscopy (AFM), scanning force microscopy (SEM), Raman spectroscopy, X-ray diffraction (XRD), optical emission spectrometer (OES), Ultraviolet Visible NearInfrared (UV-Vis-NIR) spectroscopy, X-ray photoelectron spectroscopy (XPS), and Hall measurement techniques can be used for the evaluation of the prepared functional thin films.

Acknowledgment:

The authors would like to thank Professor Dr. YasunoriOhtsu and Professor Dr. Tooru Tanaka, Graduate School of Science and Engineering, Saga University, Japan for supervisions, guidelines, and fruitful discussions. Moreover, Dr. Hossain extends his gratitude to K. Ikari, Y. Takada, T. Ide, Y. Nakamura, and K. Sugawara Graduate School of Science and Engineering, Saga University, Saga, 840-8502, Japan for their comments and suggestions and for technical assistance.

Availability of Data: The data that support the findings of this study are available from the corresponding author upon reasonable request.

Ethical Responsibility of Authors: The authors declare the Ethical Responsibility of Authors.

Conflicts of Interests: The authors declare there are no conflicts of interests and no competing interests.

References

- [1] F. F. Chen, J. P. Chang, "Lecture Notes on Principles of Plasma Processing", Plenum, New York, 2002.
- [2] M. A. Lieberman, A. J. Lichtenberg, "Principles of Plasma Discharges and Material Processing", 2nd ed. John Wiley & Sons, Inc., New York, 2005.
- [3] P. Chabert, N. Braithwaite, "Physics of Radio- Frequency Plasmas", Cambridge University Press, Cambridge, 2011.

- [4] M. A. Hossain, "Development of Magnetized Plasma Sputtering Source for Effective Target Utilization with Various Magnet Setups", PhD Thesis, Graduate School of Science and Engineering, Saga University, Japan, 2018.
- [5] S. Yongkun, A. Z. Christian, R. M. Sankaran, Plasma Processes Polymer, 2020, 202000009.
- [6] P. S. Rawat, R. C. Srivastava, G. Dixit, K. Asokan, Vacuum, Vol. 182, 109700, 2020.
- [7] J. Y. Zhang, I. W. Boyd, B. J. O'sullivan, P. K. Hurley, P. V. Kelly, J. P. Senateur, Nanocrystalline TiO₂ films studied by optical, XRD and FTIR spectroscopy. Journal of Non-Crystalline Solids, 303(1), pp.134-138, 2002
- [8] M. A. M. Patwary, K. Saito, Q. Guo, T. Tanaka, Thin Solid Films, 675, 59 (2019).
- [9] M. A. M. Patwary, C. Y. Ho, K. Saito, Q. Guo, K. M. Yu, W. Walukiewicz, T. Tanaka, J. Appl. Phys., 127 (2020) 085302.
- [10] D. J. Gardiner, Practical Raman spectroscopy, Springer-Verlag., 1989, ISBN 978-0-387-50254-0.
- [11] B. C. Ghos, S. F. U. Farhad, M. A. M. Patwary, S. Majumder, M. A. Hossain, N. I. Tanvir, M. A. Rahman, T. Tanaka, Q. Guo, J. ACS Omega, 6(4) (2021) 2665-2674.
- [12] S. F. U. Farhad, M. A. Hossain, N. I. Tanvir, R. Akter, M. A. M. Patwary, M. Shahjahan, M. A. Rahman, J. Materials Science in Semiconductor Processing, 95 (2019) 68-75
- [13] S. F. U. Farhad, S. Majumder, M. A. Hossain, N. I. Tanvir, R. Akter, M. A. M. Patwary, J. MRS Advances, 4 (16) (2019) 937-944
- [14] M. A. M. Patwary, M. Ohishi, K. Saito, Q. Guo, K. M. Yu, T. Tanaka, ECS J. Sol. State Science and Technology, 10 (2021) 065019.
- [15] Y. Ohtsu, S. Tsuruta, T. Tabaru, and M. Akiyama, Surface Coatings Technology, 307, 1134–1138, 2016.
- [16] T. Ide, M. A. Hossain, Y. Nakamura, and Y. Ohtsu, Journal of Vacuum Sci. Technol. A: Vacuum, Surfaces, and Films, 35, 061312, 2017.
- [17] Y. Ohtsu and T. Yanagise, Plasma Sources Sci. Technol., 24, 034005, 2015.
- [18] Y. Ohtsu, N. Matsumoto, J. Schulze, and E. Schuengel, Phys. Plasmas 23, 033510, 2016.
- [19] M. A. Hossain, T. Ide, K. Ikari, and Y. Ohtsu, Vacuum, 128, pp. 219-225, 2016.
- [20] M. A. Hossain, Y. Ohtsu, and T. Tabaru, Plasma Chem. Plasma Process., vol. 37, pp. 1663–1677, 2017.
- [21] M. A. Hossain, Y. Ohtsu, Jpn. J. Appl. Phys., vol. 57, 01AA05, 2018.
- [22] M. A. Hossain, Y. Ohtsu, IEEE Transaction on Plasma Sci., vol. 46, no. 8, August 2018.
- [23] T. Sumiyama, T. Fukumoto, Y. Ohtsu, T. Tabaru, AIP Advances 7, 055310, 2017.
- [24] Y. Ohtsu, T. Nakashima, R. Tanaka, J. Schulze, Vacuum, vol. 181, 109593, Nov. 2020.
- [25] Y. Ohtsu, S. Imoto, S. Takemura, J. Schulze, Vacuum, vol. 193, 110531, Nov. 2021.
- [26] http://laacg.lan.gov/laacg/services/serv_codes.phtml.